

Losses Minimization Control for an Integrated Multidrive Topology Devoted to Hybrid Electric Vehicles

Giovanni Nobile , *Student Member, IEEE*, Giacomo Scelba , *Senior Member, IEEE*, Mario Cacciato , *Member, IEEE*, and Giuseppe Scarcella, *Senior Member, IEEE*

Abstract—This paper deals with the study and implementation of a losses minimization control strategy for an integrated multidrive (IMD) topology used in the drivetrain of parallel hybrid electric vehicles. In this IMD, the stator sections of a multiwinding induction machine are interfaced to the storage units through standard three-phase inverters. The goal of this study is to optimize the management of multidirectional power flows in an IMD configuration, reducing both the power losses of the induction machine and the energy storage units while keeping the computational complexity suitably low. To this aim, the proposed approach consists in a control strategy that continuously searches for the best compromise between the torque response and the power capability of each storage unit while minimizing the overall power losses. Using such an approach, a significant improvement in the overall efficiency is obtained. Simulations and experimental tests confirm the effectiveness of the proposed method.

Index Terms—Automotive, energy efficiency, hybrid electric vehicles (HEVs), hybrid energy storage, induction motor drives, maximum torque per ampere (MTPA), multiwinding motor drives, starter alternator.

NOMENCLATURE

ω, ω_{rm}	Angular speed of the $qd0$ reference frame and mechanical rotor speed.
$v_{qs}, i_{qs}, \lambda_{qs}$	q -axis stator voltage, current, and flux.
$v_{ds}, i_{ds}, \lambda_{ds}$	d -axis stator voltage, current, and flux.
i_{qsj}, i_{dsj}	q -axis and d -axis components of the current in the j th sub-machine.
I_{sj}	Peak value of the stator current in the j th sub-machine.
R_s, L_{ls}	Stator resistance and leakage inductance.
R'_r, L'_{lr}	Rotor resistance and leakage inductance.

L_M	Magnetizing inductance.
R_{fe}	Stator iron resistance.
$\omega_{s\lambda r}$	Slip angular frequency under field orientation.
$\theta_{\lambda r}$	Rotor flux angular position.
$t_r = L'_r/R'_r$	Rotor time constant.
T_e	Electromagnetic torque.
\bar{p}	Number of pole pairs.
SOC	State of charge.
SOH	State of health.
$C_{\text{sc, cell}}, v_{\text{sc}}$	Capacitance and actual voltage of a single cell of the supercapacitor string.
n_{sc}	Number of series-connected supercapacitor cells.
Δt	Horizon time.
v_{sc}	Supercapacitor string voltage.
$v_{\text{sc, max}}$	Maximum voltage of the supercapacitor string.
v_{bt}	Battery pack voltage.
E_0, R_i	No-load voltage and internal resistance of the battery pack.
PC	Power capability.
C_{bt}	Rated capacity of the battery.
R_{sc}	Internal resistance of the supercapacitor.
λ_m	Air-gap flux.
λ_{qm}	q -axis component of the air-gap flux.
λ_{dm}	d -axis component of the air-gap flux.
λ_{dr}	Amplitude of the rotor flux under field orientation.
λ	Lagrange multiplier.
$T_{e, \text{demand}}$	Torque demand.
P_m	Mechanical power.
V_{as1}	Peak value of the motor phase voltage in stator 1.
V_{as2}	Peak value of the motor phase voltage in stator 2.
$v_s, V_{s\text{max}}$	Phase voltage in ac side of inverters and its maximum value.
φ_1, φ_2	Phase angles between voltages and currents in sub-machines 1 and 2.
ω_e	Synchronous angular speed.
i_{cap}	Current in dc-link capacitor bank.
η	Efficiency of the integrated multidrive system.
HEV	Hybrid electric vehicles.
SM	Sub-machine.

Manuscript received January 30, 2018; revised June 23, 2018 and August 20, 2018; accepted September 26, 2018. Date of publication December 10, 2018; date of current version June 28, 2019. This work was partially supported by the Italian Ministry for Economic Development (MISE), under the project “M9”-C32F18000100008. (Corresponding author: Giacomo Scelba.)

The authors are with the Electrical, Electronics and Computer Science Department, University of Catania, 95125 Catania, Italy (e-mail: giovanni.nobile@dieei.unict.it; giacomo.scelba@dieei.unict.it; mario.cacciato@dieei.unict.it; giuseppe.scarcella@dieei.unict.it).

Color versions of one or more of the figures in this paper are available online at <http://ieeexplore.ieee.org>.

Digital Object Identifier 10.1109/TIE.2018.2875633

VSI	Voltage source inverter.
VRLA	Valve-regulated lead–acid batteries.
ICE	Internal combustion engine.
IFOC	Indirect field oriented control.

I. INTRODUCTION

NOWADAYS, environmental benefits of using HEVs are well known. Compared with the traditionally powered vehicle, which have undergone continuous enhancement in recent decades, further significant development steps are still necessary for the market acceptance of the next generation of HEVs. This involves the development of new technologies, methodologies, and devices involving specific electrical and electronic engineering fields.

One of the key aspects is strictly related with the power conversion efficiency boosting for HEVs as it directly impacts the vehicle operating range. In particular, focusing on the electric drive system, a large number of scientific contributions dealing with innovative control strategies for the optimal energy management and losses minimization have been proposed in past literature, for example, [1]–[3]. Among those, many papers are mainly focused on the electric machine deeply investigating its efficiency [4]–[7], but a comprehensive losses evaluation including the storage units has not been provided yet.

Referring to the electrical machine, the idea of splitting the stator windings in several sets has been investigated in the literature, with the goal to share among different subunits the total power required to drive the load [8]–[13]. In particular, the model of the electrical machine with multiple stator winding sets has been presented and simulated in [8] and [9], whereas a particular dual stator winding induction machine drive was described in [10], leading to two submachines with a dissimilar number of poles. In [11], a direct rotor-field oriented control has been implemented for an induction motor having two sets of stator windings spatially shifted by 30 electrical degrees. Moreover, a new current control scheme has been introduced to compensate for the drive asymmetries as the currents of the two stator winding sets are independently controlled.

The circulating currents generated by the non-sinusoidal air-gap flux distribution in multiple three-phase stator windings have been also investigated in [12]. A review on control methods for power sharing among winding sets of multiple three-phase machines was provided in [13].

While the integration of three-phase motor drives in automotive applications is very widespread [14]–[20], a limited number of scientific contributions dealt with the use of multiple three-phase stator winding motor drives intended for an HEV; some examples are described in [21]–[24]. In particular, a loss minimization control algorithm has been presented in [23] for a multiwinding induction machine inserted in parallel to HEV drivetrains, addressing an integrated multidrive (IMD) topology where the stators are interfaced to the storage units through standard three-phase inverters, see Fig. 1. The stator windings of the electrical machine have no spatial shift. The analysis of [23] highlights the aptitude of the control strategy to set a multidirectional power flow and track the minimum losses operating point under a constant magnetizing flux condition. Moreover,

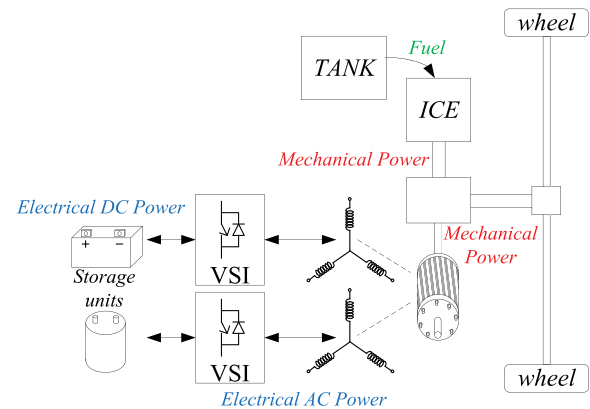


Fig. 1. HEV parallel drivetrain including a multiwinding induction machine.

only a preliminary validation of the proposed approach is provided, limited to a few operating scenarios.

Under this perspective, this paper provides a more comprehensive study and implementation of the loss minimization control algorithm given in [23]; in particular, an efficiency optimization current profile is included in the mathematical treatment, leading to the modulation of the total magnetizing flux as a function of the load conditions. Moreover, a detailed experimental validation of the proposed approach is presented, confirming the capability of the method to properly track the actual minimum power loss of the IMD. Finally, losses distribution in the IMD has been also evaluated.

Causing only a low increment of the computational burden, such a challenging algorithm would be able to ensure high control flexibility while keeping minimum system losses of electrical machine and storage units in every operating condition. Although the proposed approach is of general validity, it has been applied to a parallel drivetrain of an HEV using a hybrid storage system including different storage unit technologies, e.g., supercapacitors and lithium-ion batteries. Moreover, different than the conventional approach, where the hybrid energy storage systems (HESS) are connected to a common dc bus by means of dc–dc power converters, parallel power flows are independently handled in the proposed drive configuration. The latter configuration implies some advantages in terms of system reliability in comparison to the conventional one [2], [24]. The losses minimization profiles are determined exploiting a suitable modeling of the energy storage units and electrical machine; these profiles are integrated in a vector control strategy allowing the independent control of the sub-units composing the electrical machine in a simple but effective way. Furthermore, the conditions for optimal operating points are determined in order to comply with some technical constraints, in terms of PC assessment and manufacturer recommendations that could affect the state of health of the storage units.

This paper is structured as follows. Section II describes the analytical model of each part composing the IMD and the vector control strategy. The analytical formulation of power losses is reported in Section III. Section IV shows the proposed power losses minimization strategy, whereas Section V addresses the numerical simulations and experimental validation.

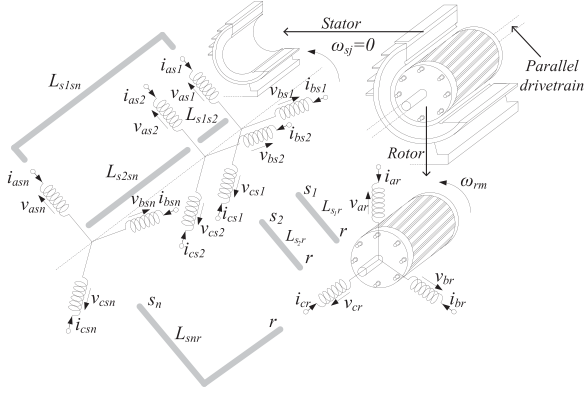


Fig. 2. Schematical representation of the three-phase sub-machines.

II. IMD TOPOLOGY MODELING

Many losses minimization methods require a proper modeling of the system. For the proposed method, the current control loop structure and the models used to calculate the power losses in the electrical machine and storage units are below described.

A. Current Vector Control Strategy

The IMD configuration used in this study is achieved considering the stator-distributed winding of a standard squirrel cage induction machine split into different three-phase sub-windings without spatial shift (see Fig. 2) with the constrain to obtain the same magnetomotive force distribution of a standard machine [24], [25]. Each winding has a different number of turns N_j depending on the desired back electromotive force, whereas the wires cross section is related to the rated currents.

The total magnetic airgap flux and torque generated in the electromagnetic system can be approximated (under the assumption of a linear system) as the sum of the contributions provided by each fictitious sub-machine, consisting of one of the sub-windings and sharing the same rotor. This electromagnetic multiwinding system allows us to supply storage units featuring different power capabilities with different dc voltage levels by means of standard three-phase voltage source inverters, each one feeding a single SM. According to [23] and [24], the IMD can be controlled by implementing field oriented control algorithms in the SMs, which are coupled by the total rotor flux. A common qd reference frame is used for all the drive quantities. The field orientation is obtained by imposing the total slip angular frequency $\omega_{s\lambda r}$ according to (1), whereas the rotor flux angular position $\theta_{\lambda r}$ is calculated from $\omega_{s\lambda r}$ and from the rotor speed ω_{re} , as in (2).

$$\omega_{s\lambda r} = \frac{1}{\tau_r} \cdot \frac{(i_{qs1} + i_{qs2} + \dots + i_{qsn})}{(i_{ds1} + i_{ds2} + \dots + i_{dsn})}$$

$$i_{qs} = i_{qs1} + i_{qs2} + \dots + i_{qsn}$$

$$i_{ds} = i_{ds1} + i_{ds2} + \dots + i_{dsn}$$

$$\theta_{\lambda r} = \theta_{\lambda r0} + \int (\omega_{s\lambda r} + \omega_{re}) dt$$

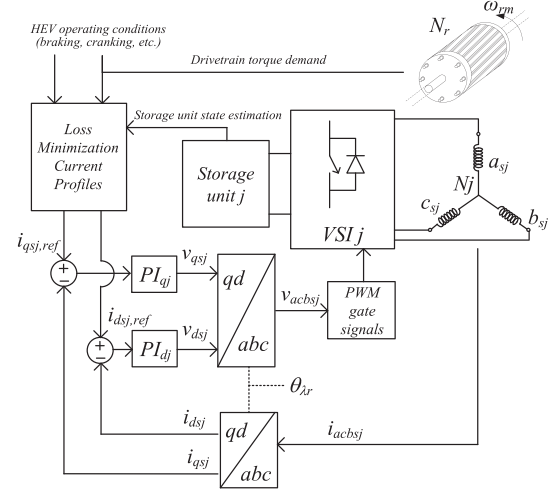


Fig. 3. Block diagram of the IFOC implemented in the j th SM.

where τ_r is the rotor time constant and i_{qsj} and i_{dsj} are, respectively, the torque and flux components of the stator currents flowing in the j th SM. i_{qs} and i_{ds} are the total torque and flux producing components of the induction machine.

The relationship (1) has been obtained by assuming constant or slowly variable amplitude of the rotor flux. It is worth noting that in this analytical formulation, the electrical quantities associated with the j th stator winding and to the rotor are referred to the reference stator winding 1 through the turns ratio N_1/N_j and N_1/N_r , respectively.

The electromagnetic torque provided by the IMD can be expressed as the sum of the torque contributions provided by each SM as follows:

$$\begin{aligned} T_e &= \frac{P_m}{\omega_{rm}} = \frac{3}{2} \bar{p} (i_{qs1} + \dots + i_{qsn}) \lambda_{dr} \\ &= \frac{3}{2} \bar{p} L_M (i_{qs1} + \dots + i_{qsn}) \cdot (i_{ds1} + \dots + i_{dsn}) \\ &= T_{e1} + \dots + T_{en} \end{aligned} \quad (3)$$

where

$$T_{ej} = \frac{3}{2} \bar{p} L_M i_{qsj} (i_{ds1} + \dots + i_{dsn}). \quad (4)$$

Therefore, the torque produced by the n integrated machines is proportional to the algebraic sum of the torque components i_{qsj} . Likewise, the amplitude of the flux is proportional to the algebraic sum of the flux components i_{dsj} . Fig. 3 shows a block diagram of the IFOC implemented for the j th SM. The current loop allows us to perform the decoupled torque and flux control in each SM. The reference currents must be assigned in order to improve the overall system efficiency, considering the operative scenario (braking, cranking, etc.) and the actual state of the storage units, as detailed in the following.

This IMD topology allows us to set multidirectional power flows among the mechanical system and the stator units. Moreover, some energy can flow among the storage units while the mechanical power is kept constant. In other words, the IMD is able to handle multidirectional power flows by simply

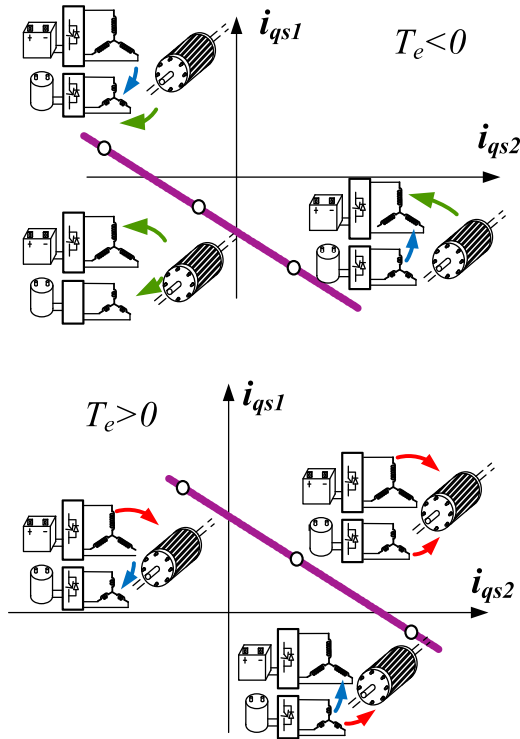


Fig. 4. Power flows in the IMD system.

controlling the qd stator current components of the SMs composing the IMD.

A graphical representation of the torque expression (4) for an IMD including two energy storage units and operating at constant speed is shown in Fig. 4. It can be observed that different power path flows can be forced in the IMD just by properly setting the currents i_{qsj} .

As infinite combinations of torque and flux current components allow us to establish the same working condition of the electrical machine, additional constraints in the reference currents have to be defined in order to achieve a specific goal, for example, the actual PC of the storage units connected to the dc side of each drive. In this study, the efficiency maximization of the power conversion process is pursued while keeping limited computational burden and satisfying dynamic behavior.

B. HESS Modeling

Arrays of supercapacitors and series-connected batteries (lithium ions and VRLA battery technologies) have been considered as storage units for the HEV parallel drivetrain. They have been properly modeled in order to allow a straightforward online monitoring of their SOC and PC while keeping good accuracy and low computational complexity. SOC and PC are crucial quantities to assess the suitable energy management in the whole IMD system.

As proposed by several authors and supercapacitor manufacturers, the most straightforward approach to model the supercapacitors strings (sc) is to consider a simple resistor-capacitor network constituted by the series of a capacitor C_{sc} and a resistor R_{sc} [26]. The parameters C_{sc} and R_{sc} can be easily identified

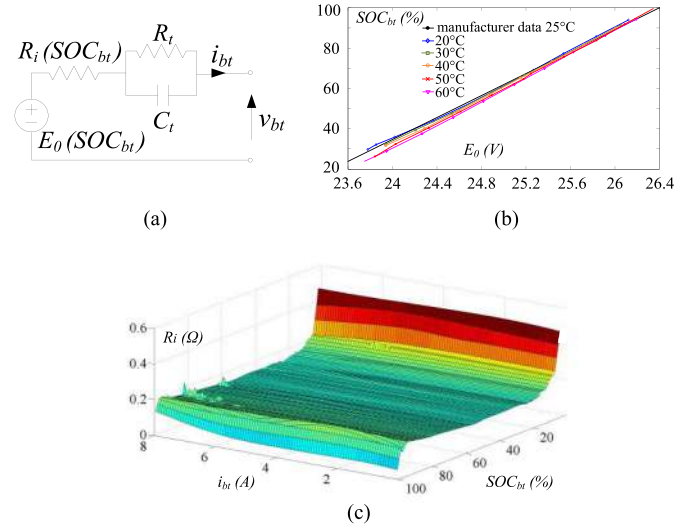


Fig. 5. (a) Thevenin equivalent circuit used to model the battery behavior. (b) Example of $E_0(SOC_{bt})$ curve for a 24-V 108-Ah VRLA battery. (c) Example of $R_i(SOC_{bt}, i_{bt})$ curve for a 24-V 108-A-h VRLA battery.

using data provided by the manufacturer of the supercapacitor cells, and given as follows:

$$C_{sc} = C_{sc,cell} / n_{sc} \quad v_{sc} = v_{sc,cell} \cdot n_{sc}$$

$$R_{sc} = R_{sc,cell} \cdot n_{sc} \quad v_{sc,rated} = v_{sc,cell,rated} \cdot n_{sc} \quad (5)$$

The actual SOC of the supercapacitor SOC_{sc} is given by the ratio between the actual voltage v_{sc} and the maximum voltage $v_{sc,max}$ [3]. Generally, the maximum value of voltage $v_{sc,max}$ is assigned equal to the rated one. Moreover, during normal operation, the SOC_{sc} is usually maintained between $35 \div 40\%$ ($SOC_{sc,min}$) and 95% ($SOC_{sc,max}$) [2].

The PC of the supercapacitor during the discharge process is a function of the actual SOC_{sc} and of the selected horizon time Δt , which depends on the actual operating scenario of the drivetrain (acceleration, engine cranking, etc.) [26]

$$PC_{sc,ds} = i_{sc,ds,PC} \cdot \left(SOC_{sc} - \left| \frac{SOC_{sc} - SOC_{sc,min}}{2} \right| \right) \cdot v_{sc,max} \quad (6)$$

where $i_{sc,ds,PC}$ is the maximum value of the current that can be imposed during the discharge process, expressed as a function of the actual SOC_{sc} and minimum $SOC_{sc,min}$

$$i_{sc,ds,PC} = \frac{SOC_{sc} - SOC_{sc,min}}{\Delta t} v_{sc,max} \cdot C_{sc} \quad (7)$$

Same formulation can be adopted for the charging process.

Different than supercapacitors, modeling of batteries (bt) is more complicated due to several nonlinear phenomena occurring during charging and discharging processes. Hence, an accurate estimation of SOC_{bt} is often a difficult task [27]. In this study, the battery pack has been modeled with the equivalent electric circuit represented in Fig. 5, where the no-load voltage E_0 and the internal resistance R_t depend on the actual SOC_{bt} .

It can be observed from Fig. 5(c) that the current rate has a negligible effect on the R_i value. The parameters R_t and C_t are

used to describe the dynamic behavior of the battery [27]. The identification of these parameters can be performed as reported in [28]. However, to get a satisfactory accuracy, such parameters need to be continuously tuned by using an estimation algorithm capable to also provide the actual value of SOC_{bt} . In this paper, a proportional-integral (PI)-based observer has been exploited to carry out the value of SOC_{bt} [28].

The value of power that can be continuously delivered to the battery without exceeding the SOC_{bt} limits during the discharge, and considering a given time horizon Δt , can be predicted as follows [29]:

$$\text{PC}_{\text{bt},ds} = v_{\text{bt},\min} \cdot i_{\text{bt},ds,PC} \quad (8)$$

$$i_{\text{bt},ds,PC} = \frac{\text{SOC}_{\text{bt}} - \text{SOC}_{\text{bt},\min}}{\Delta t} \cdot \text{SOH} \cdot C_{\text{bt}} \quad (9)$$

where C_{bt} is the rated capacity of the battery. A similar formulation can be reported about the charging process, where an appropriate efficiency index depending on actual SOC_{bt} and on typical discharge rate is introduced in (8) [30]. The charge process can be also related to the charge current recommended by the battery manufacturer pursuing the objective to extend the lifetime of the storage unit. It leads to a minimum charging current $i_{\text{bt},ch}$ usually lower than the one calculated from PC assessment $i_{\text{bt},ch,PC}$.

III. POWER LOSSES MODEL

The overall system power losses minimization is obtained by defining specific current profiles, which must be compliant to the SOC and PC constraints. The basic principle of any losses reduction approach is to determine the optimal currents and the flux magnitude so that minimum losses occur, maintaining the desired electromagnetic torque. For the sake of clarity, hereafter an IMD using two units has been considered.

The mathematical loss expression from the full loss model of an induction motor is a very complex and onerous job [31]–[33]. In this paper, an induction motor model including iron loss is exploited, where iron losses are modeled by a resistor R_{fe} that is inserted in parallel to the magnetizing branch so that the power losses depend on the air-gap flux linkage. This solution can be considered a good compromise between accuracy and computational burden.

By neglecting the losses associated with the power converters and dc bus capacitors, the total power losses $\sum P_l$ in the IMD can be expressed as in the following:

$$\sum P_l = P_{l,sc} + P_{l,bt} + P_{js1} + P_{js2} + P_{jr} + P_{\text{fe}}. \quad (10)$$

The power loss $P_{l,sc}$ is associated with the internal resistance R_{sc} of the supercapacitors given by

$$P_{l,sc} = R_{sc} \cdot i_{sc}^2. \quad (11)$$

The current i_{sc} can be expressed as a function of the currents i_{qs2} and i_{ds2} flowing into the corresponding stator unit, by imposing the equality between the active powers in the ac and

dc sides of the inverter

$$i_{sc} = K_{sc} \cdot \sqrt{i_{qs2}^2 + i_{ds2}^2} \Rightarrow P_{l,sc} = R_{sc} \cdot K_{sc}^2 \cdot (i_{qs2}^2 + i_{ds2}^2) \quad (12)$$

where K_{sc} is given by

$$K_{sc} = \frac{3 \cdot V_{as2} \cdot \cos \phi_2}{v_{sc} \cdot \sqrt{2}}. \quad (13)$$

The losses associated with the battery packs can be evaluated in a similar way, considering the joule losses of the resistive elements

$$P_{l,bt} = (R_i(\text{SOC}_{\text{bt}}) + R_t) \cdot i_{\text{bt}}^2. \quad (14)$$

The actual value of the resistance R_i depends on SOC_{bt} [28]. Similarly, the battery current i_{bt} can be expressed as a function of the current components i_{qs1} and i_{ds1} as follows:

$$i_{\text{bt}} = K_{bt} \cdot \sqrt{i_{qs1}^2 + i_{ds1}^2} \Rightarrow P_{l,bt} = (R_i + R_t) \cdot K_{bt}^2 \cdot (i_{qs1}^2 + i_{ds1}^2) = R_{bt} \cdot K_{bt}^2 \cdot (i_{qs1}^2 + i_{ds1}^2) \quad (15)$$

where

$$K_{bt} = \frac{3 \cdot V_{as1} \cdot \cos \phi_1}{v_{bt} \cdot \sqrt{2}}. \quad (16)$$

The copper losses in the stators of both the SMs can be calculated as follows:

$$P_{js1} = 3 \cdot R_{s1} \cdot I_{as1}^2 = \frac{3}{2} \cdot R_{s1} \cdot (i_{qs1}^2 + i_{ds1}^2) \quad (17)$$

$$P_{js2} = 3 \cdot R_{s2} \cdot I_{as2}^2 = \frac{3}{2} \cdot R_{s2} \cdot (i_{qs2}^2 + i_{ds2}^2). \quad (18)$$

Under the assumption of rotor flux orientation, which is imposed by the control algorithm, the copper losses in the rotor can be approximated as follows [5], [34]:

$$P_{jr} \cong \frac{3}{2} \cdot R_r \cdot I_{qr}^2 = \frac{3}{2} \cdot R_r \cdot \frac{L_M^2}{L_r^2} \cdot (i_{qs1} + i_{qs2})^2. \quad (19)$$

The rotor iron loss is quite small compared to the stator iron loss. Hence, by neglecting the rotor iron loss, P_{fe} can be expressed as follows [31], [35], [36]:

$$P_{\text{fe}} \cong P_{\text{fes}} \Rightarrow P_{\text{fes}} \cong \frac{\omega_e^2 \cdot \lambda_m^2}{R_{\text{fe}}} \quad (20)$$

where λ_m is the air-gap flux. The field orientation condition leads to the following:

$$\begin{cases} \lambda_{qm} \cong 0 \\ \lambda_{dm} \cong \lambda_{dr} \end{cases} \Rightarrow P_{\text{fe}} \cong \frac{\omega_e^2 \cdot \lambda_{dr}^2}{R_{\text{fe}}} \quad (21)$$

where λ_{dr} is the amplitude of the rotor flux and is given by

$$\lambda_{dr} = L_{lr} \cdot i_{dr} + L_M \cdot i_{dm}. \quad (22)$$

Some mathematical manipulations are then performed aimed at tailoring a representation of λ_{dr} only depending on the stator current components

$$\lambda_{dr} = \frac{L_{lr} \left(1 + \frac{L_M \cdot L_r}{K_\delta} \right) \cdot i_{ds} + \frac{\omega_e \cdot L_M^2 \cdot L_{lr}^2}{R_{\text{fe}} \cdot K_\delta} \cdot i_{qs}}{\left(1 - \frac{L_M \cdot L_r}{K_\delta} \right)} \quad (23)$$

where

$$K_\delta = \frac{\omega_e^2 \cdot L_M^2 \cdot L_{lr}^2}{R_{fe}^2} + L_r^2. \quad (24)$$

The contribution given by the presence of i_{qs} in the expression of the rotor flux is quite small due to the high value of R_{fe} . The iron losses P_{fe} can be expressed as

$$\begin{aligned} P_{fe} &\cong \frac{\omega_e^2 \cdot \lambda_{dr}^2}{R_{fe}} = \frac{\omega_e^2}{R_{fe}} \cdot (K_\alpha \cdot i_{ds} + K_\beta \cdot i_{qs})^2 \\ &= \frac{\omega_e^2}{R_{fe}} \cdot (K_\alpha^2 \cdot i_{ds}^2 + K_\beta^2 \cdot i_{qs}^2 + 2 \cdot K_\alpha \cdot K_\beta \cdot i_{ds} \cdot i_{qs}) \end{aligned} \quad (25)$$

where

$$K_\alpha = \frac{\left(L_{lr} + \frac{L_M \cdot L_r \cdot L_{ls}}{K_\delta}\right)}{\left(1 - \frac{L_M \cdot L_r}{K_\delta}\right)} \quad K_\beta = \frac{\frac{\omega_e \cdot L_M^2 \cdot L_{lr}^2}{R_{fe} \cdot K_\delta}}{\left(1 - \frac{L_M \cdot L_r}{K_\delta}\right)}. \quad (26)$$

The power loss P_{fe} given by (25) can be rewritten as a function of the currents i_{qs1} , i_{qs2} , i_{ds1} , and i_{ds2}

$$\begin{aligned} i_{qs} &= i_{qs1} + i_{qs2} \\ i_{ds} &= i_{ds1} + i_{ds2} \\ P_{fe} &= \frac{\omega_e^2}{R_{fe}} \cdot K_\alpha^2 \cdot i_{ds1}^2 + \frac{\omega_e^2}{R_{fe}} \cdot K_\alpha^2 \cdot i_{ds2}^2 \\ &\quad + 2 \cdot \frac{\omega_e^2}{R_{fe}} \cdot K_\alpha^2 \cdot i_{ds1} \cdot i_{ds2} + \frac{\omega_e^2}{R_{fe}} \cdot K_\beta^2 \cdot i_{qs1}^2 \\ &\quad + \frac{\omega_e^2}{R_{fe}} \cdot K_\beta^2 \cdot i_{qs2}^2 + 2 \cdot \frac{\omega_e^2}{R_{fe}} \cdot K_\beta^2 \cdot i_{qs1} \cdot i_{qs2} \\ &\quad + 2 \cdot \frac{\omega_e^2}{R_{fe}} \cdot K_\alpha \cdot K_\beta \cdot i_{qs1} \cdot i_{ds1} \\ &\quad + 2 \cdot \frac{\omega_e^2}{R_{fe}} \cdot K_\alpha \cdot K_\beta \cdot i_{qs2} \cdot i_{ds1} \\ &\quad + 2 \cdot \frac{\omega_e^2}{R_{fe}} \cdot K_\alpha \cdot K_\beta \cdot i_{qs1} \cdot i_{ds2} \\ &\quad + 2 \cdot \frac{\omega_e^2}{R_{fe}} \cdot K_\alpha \cdot K_\beta \cdot i_{qs2} \cdot i_{ds2}. \end{aligned} \quad (27)$$

The last relationship (28) is acceptable for the calculation of the minimum power losses. Furthermore, (28) has the advantage of being relatively simple, compared to other iron losses models that are more accurate but require a higher number of motor parameters [31].

Finally, the total system power losses can be expressed as follows:

$$\begin{aligned} \sum P_l &= P_{l,sc} + P_{l,bt} + P_{js1} + P_{js2} + P_{jr} + P_{fe} \\ &= R_{sc} \cdot K_{sc}^2 \cdot (i_{qs2}^2 + i_{ds2}^2) + R_{bt} \cdot K_{bt}^2 \cdot (i_{qs1}^2 + i_{ds1}^2) \\ &\quad + \frac{3}{2} \cdot R_{s1} \cdot (i_{qs1}^2 + i_{ds1}^2) + \frac{3}{2} \cdot R_{s2} \cdot (i_{qs2}^2 + i_{ds2}^2) \\ &\quad + \frac{3}{2} \cdot R_r \cdot \frac{L_M^2}{L_r^2} (i_{qs1} + i_{qs2})^2 + P_{fe}. \end{aligned} \quad (29)$$

IV. POWER LOSS MINIMIZATION PROFILES

The qd currents set minimizing the model losses function (29) can be determined by using the method of Lagrange multipliers [37], [38]. In the following, an analysis is assumed that the drive is operating at steady state, thus the total torque and flux producing components i_{qs} and i_{ds} are constants.

The first step is to detect the stationary points for which the total power loss is minimum. In particular, an analytical solution can be found by solving the following system:

$$\begin{aligned} L(i_{qs1}, i_{qs2}, i_{ds1}, i_{ds2}, \lambda) &= \sum P_l - \lambda \cdot g(i_{qs1}, i_{qs2}, i_{ds1}, i_{ds2}) \\ \nabla L(i_{qs1}, i_{qs2}, i_{ds1}, i_{ds2}, \lambda) &= 0 \\ \Rightarrow \begin{cases} f_{x_1} = \frac{\partial L}{\partial i_{qs1}} = 0; f_{x_2} = \frac{\partial L}{\partial i_{qs2}} = 0; f_{x_3} \\ = \frac{\partial L}{\partial i_{ds1}} = 0; f_{x_4} = \frac{\partial L}{\partial i_{ds2}} = 0 \\ \frac{\partial L}{\partial \lambda} = 0 \end{cases} \end{aligned} \quad (30)$$

where g represents the constraints set

$$\begin{aligned} g(i_{qs1}, i_{qs2}, i_{ds1}, i_{ds2}) &= \begin{cases} i_{qs1} + i_{qs2} = i_{qs} \\ i_{ds1} + i_{ds2} = i_{ds} \\ i_{qs} \cdot i_{ds} = \frac{T_e}{\frac{3}{2} \cdot p \cdot L_M} = K \end{cases} \\ \Rightarrow g(i_{qs1}, i_{qs2}, i_{ds1}, i_{ds2}) &= i_{qs1} \cdot i_{ds1} + i_{qs1} \cdot i_{ds2} + i_{qs2} \cdot i_{ds1} + i_{qs2} \cdot i_{ds2} - K \end{aligned} \quad (31)$$

and λ is the Lagrange multiplier. The solution of (30), under the constraints given by (31), leads to the identification of the stationary points, which in this case correspond to a single set of currents i_{qs1}^* , i_{qs2}^* , i_{ds1}^* , and i_{ds2}^*

$$\begin{cases} i_{qs1}^* = \frac{K_2}{K_1 + K_2} \cdot i_{qs} = \frac{2 \cdot R_{sc} \cdot K_{sc}^2 + 3 \cdot R_{s2}}{2 \cdot R_{bt} \cdot K_{bt}^2 + 3 \cdot R_{s1} + 2 \cdot R_{sc} \cdot K_{sc}^2 + 3 \cdot R_{s2}} \cdot i_{qs} \\ i_{qs2}^* = \frac{K_1}{K_1 + K_2} \cdot i_{qs} = \frac{2 \cdot R_{bt} \cdot K_{bt}^2 + 3 \cdot R_{s1}}{2 \cdot R_{bt} \cdot K_{bt}^2 + 3 \cdot R_{s1} + 2 \cdot R_{sc} \cdot K_{sc}^2 + 3 \cdot R_{s2}} \cdot i_{qs} \\ i_{ds1}^* = \frac{K_2}{K_1 + K_2} \cdot i_{ds} = \frac{2 \cdot R_{sc} \cdot K_{sc}^2 + 3 \cdot R_{s2}}{2 \cdot R_{bt} \cdot K_{bt}^2 + 3 \cdot R_{s1} + 2 \cdot R_{sc} \cdot K_{sc}^2 + 3 \cdot R_{s2}} \cdot i_{ds} \\ i_{ds2}^* = \frac{K_1}{K_1 + K_2} \cdot i_{ds} = \frac{2 \cdot R_{bt} \cdot K_{bt}^2 + 3 \cdot R_{s1}}{2 \cdot R_{bt} \cdot K_{bt}^2 + 3 \cdot R_{s1} + 2 \cdot R_{sc} \cdot K_{sc}^2 + 3 \cdot R_{s2}} \cdot i_{ds} \end{cases} \quad (32)$$

where

$$\begin{aligned} K_1 &= 2 \cdot R_{bt} \cdot K_{bt}^2 + 3 \cdot R_{s1} \\ K_2 &= 2 \cdot R_{sc} \cdot K_{sc}^2 + 3 \cdot R_{s2}. \end{aligned} \quad (33)$$

It is worth noting that under same torque and flux conditions (31), the presence of R_{bt} and R_{sc} in (32) can significantly modify the optimal operating point of the IMD. Such parameters are the representative of the storage unit losses. In the following section, an evaluation of the errors occurring in the determination of the minimum loss point when the storage unit losses are neglected is also provided.

Observing (32), the currents set i_{qs1}^* , i_{qs2}^* , i_{ds1}^* , and i_{ds2}^* does not depend on the iron losses parameters; this happens

because P_{fe} depends on the total q - and d -axis currents, as shown in (25), that are constants at the steady state. Hence, any combination of i_{qs1}^* , i_{qs2}^* , i_{ds1}^* , and i_{ds2}^* under the constraints set (31) leads to the same iron losses.

In (31), the flux current component i_{ds} is assumed to be established a priori, according to an efficiency optimization current profile linking the two projections of the stator current vector on the qd reference frame synchronous to the rotor flux position [32], [33], [39]–[41]. The latter shall be selected in accordance with the induction motor (IM) characteristics. If we consider a maximum torque per ampere (MTPA) control strategy, torque and flux current components are related as in (34) in the entire speed range below the rated flux, whereas $i_{ds} = i_{ds, \text{rated}}$ is imposed at higher load torques

$$i_{ds} = K_{\text{opt}} \cdot |i_{qs}|. \quad (34)$$

K_{opt} strictly depends on the motor parameters as well as on the input angular frequency [38].

Hence, the set of currents i_{qs1}^* , i_{qs2}^* , i_{ds1}^* , and i_{ds2}^* leading to the minimum losses according to (34) can be expressed as in (35), whereas (36) is valid for $i_{ds} = i_{ds, \text{rated}}$

$$\begin{cases} i_{qs1}^* = \frac{2 \cdot R_{sc} \cdot K_{sc}^2 + 3 \cdot R_{s2}}{2 \cdot R_{bt} \cdot K_{bt}^2 + 3 \cdot R_{s1} + 2 \cdot R_{sc} \cdot K_{sc}^2 + 3 \cdot R_{s2}} \cdot \frac{i_{qs}}{\sqrt{K_{\text{opt}}}} \\ i_{qs2}^* = \frac{2 \cdot R_{bt} \cdot K_{bt}^2 + 3 \cdot R_{s1}}{2 \cdot R_{bt} \cdot K_{bt}^2 + 3 \cdot R_{s1} + 2 \cdot R_{sc} \cdot K_{sc}^2 + 3 \cdot R_{s2}} \cdot \frac{i_{qs}}{\sqrt{K_{\text{opt}}}} \\ i_{ds1}^* = \frac{2 \cdot R_{sc} \cdot K_{sc}^2 + 3 \cdot R_{s2}}{2 \cdot R_{bt} \cdot K_{bt}^2 + 3 \cdot R_{s1} + 2 \cdot R_{sc} \cdot K_{sc}^2 + 3 \cdot R_{s2}} \cdot i_{ds} \cdot \sqrt{K_{\text{opt}}} \\ i_{ds2}^* = \frac{2 \cdot R_{bt} \cdot K_{bt}^2 + 3 \cdot R_{s1}}{2 \cdot R_{bt} \cdot K_{bt}^2 + 3 \cdot R_{s1} + 2 \cdot R_{sc} \cdot K_{sc}^2 + 3 \cdot R_{s2}} \cdot i_{ds} \cdot \sqrt{K_{\text{opt}}} \end{cases} \quad (35)$$

$$\begin{cases} i_{qs1}^* = \frac{2 \cdot R_{sc} \cdot K_{sc}^2 + 3 \cdot R_{s2}}{2 \cdot R_{bt} \cdot K_{bt}^2 + 3 \cdot R_{s1} + 2 \cdot R_{sc} \cdot K_{sc}^2 + 3 \cdot R_{s2}} \cdot i_{qs} \\ i_{qs2}^* = \frac{2 \cdot R_{bt} \cdot K_{bt}^2 + 3 \cdot R_{s1}}{2 \cdot R_{bt} \cdot K_{bt}^2 + 3 \cdot R_{s1} + 2 \cdot R_{sc} \cdot K_{sc}^2 + 3 \cdot R_{s2}} \cdot i_{qs} \\ i_{qs} = \frac{K}{i_{ds, \text{rated}}}; \quad i_{ds1}^* = i_{ds1, \text{rated}}; \\ i_{ds2}^* = i_{ds2, \text{rated}} \end{cases} \quad i_{ds} = i_{ds, \text{rated}}. \quad (36)$$

Under the assumption that the magnetic saturation is negligible and the drive is operating below the rated speed, the MTPA operation can be approximated to $i_{ds} = i_{qs}$, and thus the previous solutions can be written as follows:

$$\begin{cases} i_{qs1}^* = \frac{2 \cdot R_{sc} \cdot K_{sc}^2 + 3 \cdot R_{s2}}{2 \cdot R_{bt} \cdot K_{bt}^2 + 3 \cdot R_{s1} + 2 \cdot R_{sc} \cdot K_{sc}^2 + 3 \cdot R_{s2}} \cdot \sqrt{K} \\ i_{qs2}^* = \frac{2 \cdot R_{bt} \cdot K_{bt}^2 + 3 \cdot R_{s1}}{2 \cdot R_{bt} \cdot K_{bt}^2 + 3 \cdot R_{s1} + 2 \cdot R_{sc} \cdot K_{sc}^2 + 3 \cdot R_{s2}} \cdot \sqrt{K} \\ i_{ds1}^* = \frac{2 \cdot R_{sc} \cdot K_{sc}^2 + 3 \cdot R_{s2}}{2 \cdot R_{bt} \cdot K_{bt}^2 + 3 \cdot R_{s1} + 2 \cdot R_{sc} \cdot K_{sc}^2 + 3 \cdot R_{s2}} \cdot \sqrt{K} \\ i_{ds2}^* = \frac{2 \cdot R_{bt} \cdot K_{bt}^2 + 3 \cdot R_{s1}}{2 \cdot R_{bt} \cdot K_{bt}^2 + 3 \cdot R_{s1} + 2 \cdot R_{sc} \cdot K_{sc}^2 + 3 \cdot R_{s2}} \cdot \sqrt{K} \end{cases} \quad i_{qs} = i_{ds} \quad (37)$$

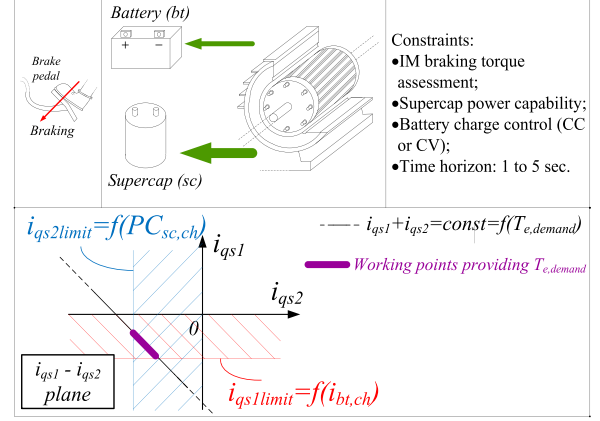


Fig. 6. Braking scenario.

$$\begin{cases} i_{qs1}^* = \frac{2 \cdot R_{sc} \cdot K_{sc}^2 + 3 \cdot R_{s2}}{2 \cdot R_{bt} \cdot K_{bt}^2 + 3 \cdot R_{s1} + 2 \cdot R_{sc} \cdot K_{sc}^2 + 3 \cdot R_{s2}} \cdot i_{qs} \\ i_{qs2}^* = \frac{2 \cdot R_{bt} \cdot K_{bt}^2 + 3 \cdot R_{s1}}{2 \cdot R_{bt} \cdot K_{bt}^2 + 3 \cdot R_{s1} + 2 \cdot R_{sc} \cdot K_{sc}^2 + 3 \cdot R_{s2}} \cdot i_{qs} \\ i_{qs} = \frac{K}{i_{ds, \text{rated}}}; \quad i_{ds1}^* = i_{ds1, \text{rated}}; \\ i_{ds2}^* = i_{ds2, \text{rated}} \end{cases} \quad i_{ds} = i_{ds, \text{rated}}. \quad (38)$$

It has been verified that the determinant of the Hessian matrix of the function $\sum P_i$ is positive, as well as the derivative term of f_{x1} in (30), i.e., f_{x1x1} , confirming that the calculated stationary point $(i_{qs1}^*, i_{qs2}^*, i_{ds1}^*, i_{ds2}^*)$ represents the minimum of the losses function; moreover, it has been verified that the last point is a global minimum.

A similar procedure could be followed to carry out the current set $(i_{qs1}^*, i_{qs2}^*, i_{ds1}^*, i_{ds2}^*)$ leading to the minimum losses for the flux-weakening operation, according to [38]; however, the last working region has not been investigated in this study.

V. SIMULATIONS AND EXPERIMENTAL VALIDATION

The proposed method has been validated in simulation and experimentally tested on a scaled test rig. Some of the main scenarios occurring during HEV real operating conditions have been included in this analysis and are shown in Figs. 6–9. It is assumed that the IMD consists of two SMs and thus includes two storage units. The value of time horizon for each scenario was assigned on the basis of statistical data coming from the main standard driving cycles [36], [42].

By assuming that the IMD is operated at an established constant flux condition, the electromagnetic torque equation provides a linear relationship between the q -axis current components, which is given as follows (31):

$$i_{qs1} + i_{qs2} = i_{qs} = \frac{T_{e, \text{demand}}}{\frac{3}{2} \bar{p} L M (i_{ds1} + i_{ds2})}. \quad (39)$$

For each working scenario of the HEV, the drive operating range can be represented by the line segment highlighted in Figs. 6–9, which is limited by the boundary torque current limits imposed according to the SOC and PC of the storage

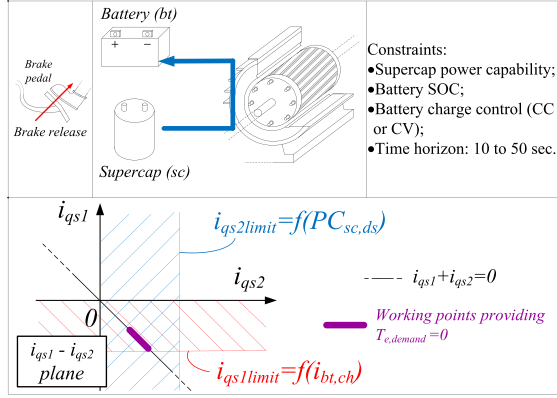


Fig. 7. Brake release scenario.

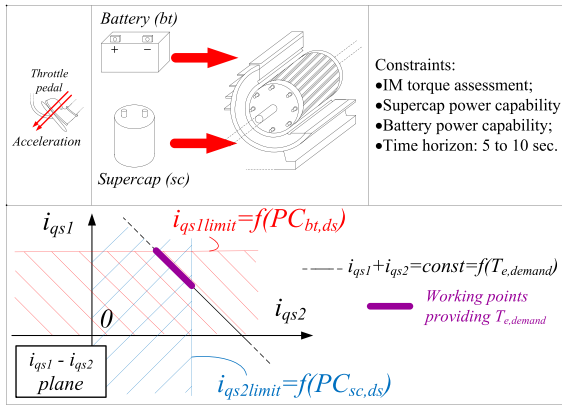


Fig. 8. Acceleration scenario.

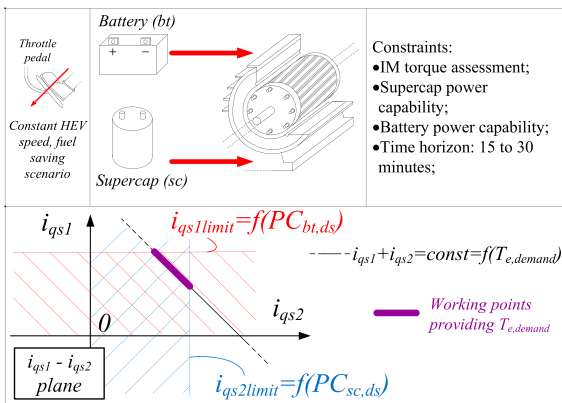


Fig. 9. Constant HEV speed, fuel saving scenario.

units. Moreover, the optimal combination of i_{qs1} , i_{qs2} , i_{ds1} , and i_{ds2} has to be chosen inside this line segment in order to minimize the system losses. If the optimal set of currents (i_{qs1}^* , i_{qs2}^* , i_{ds1}^* , i_{ds2}^*) falls off the line segment, the IMD is forced to operate at the thresholds. Whenever the flux components i_{ds1} and i_{ds2} are modified during the drive operation (i.e., because the torque demand $T_{e,demand}$ is changed), the line segment, as well as the boundary limits, will be modified in the i_{qs1} and i_{qs2} plane.

TABLE I
ELECTRICAL MACHINE AND STORAGE UNITS: MAIN TECHNICAL DATA

Multi-Winding Induction Machine 2.2 kW			
	SM_1	SM_2	
Rated Voltage (V)	266	133	
Rated Frequency (Hz)	50	50	
Rated Speed (rpm)	1470	1470	
Rated Current (A)	4.86	4.86	
Stator Resistance (Ω) @25° C	1.66	0.83	
Rotor Resistance (Ω) @25° C	1.2		
Leakage Inductance (H)	0.0065	0.0065	
Magnetizing Inductance (H)	0.14		
Iron Loss Resistance (Ω)	564		
Rotor Inertia (kg m^2)	0.009		
Battery pack (n_{bt} 24 V batteries in series)		Supercapacitor (commercial assembled module)	
Rated Voltage (V)	24	Rated Voltage (V)	160
Rated Capacity (Ah)	7.2	Total Capacity (F)	5.8
n_{bt}	19		
Technology	VRLA	Total R_{sc} (Ω)	0.475

A. Numerical Simulations

Numerical simulations have been carried out by assuming that the HESS is composed of a battery pack and a string of supercapacitors. Technical specifications of the two SMs and storage units are listed in Table I. For the sake of example, the case study “Acceleration” is focused. The boundary current limits, $i_{qs1limit}$, $i_{ds1limit}$, $i_{qs2limit}$, and $i_{ds2limit}$, can be computed by taking into consideration the actual PC of the HESS. The torque expression of the IMD must be taken into account as well

$$\begin{cases} i_{qs} \cdot i_{ds} = \frac{T_{e,demand}}{\frac{3}{2} \bar{p} L_M} = K \\ i_{qs1limit} \cdot (i_{ds1limit} + i_{ds2limit}) = f(PC_{bt,ds}) \\ i_{qs2limit} \cdot (i_{ds1limit} + i_{ds2limit}) = f(PC_{sc,ds}) \\ i_{ds1limit} = i_{ds1,rated} \quad i_{ds2limit} = i_{ds2,rated} \end{cases} \quad (40)$$

By supposing that the mechanical losses are negligible, the limits on qd currents can be calculated starting from the electromagnetic torque expression as follows:

$$i_{qs1limit} = \frac{PC_{bt,ds}}{\frac{3}{2} \cdot \bar{p} \cdot L_M \cdot \omega_{rm} \cdot i_{dslimit}} \quad (41)$$

$$i_{qs2limit} = \frac{PC_{sc,ds}}{\frac{3}{2} \cdot \bar{p} \cdot L_M \cdot \omega_{rm} \cdot i_{dslimit}} \quad (42)$$

The current limits given by (40) must also satisfy the limits related to the inverter and electrical machine current ratings

$$\begin{cases} \sqrt{i_{qs1limit}^2 + i_{ds1limit}^2} \leq i_{s1,max} \\ \sqrt{i_{qs2limit}^2 + i_{ds2limit}^2} \leq i_{s2,max} \end{cases} \quad (43)$$

The last limits correspond to a circle in the $q-d$ plane. Combining the constraints (40)–(43), it is possible to avoid that at very low speed the phase currents reach values higher than the rated ones.

In addition to the above-mentioned current constraints, voltage limits must be taken into consideration at high speeds. In particular, the maximum voltage that the inverter can synthesize is defined by the dc-link voltage and by the pulsewidth modulation (PWM) strategy. In any operating condition, the magnitude of the stator voltage vector must satisfy the following relationship:

$$v_{qs1}^2 + v_{qs2}^2 \leq v_{s,max}^2 \quad (44)$$

where $v_{s,max}$ is the maximum value of the motor phase voltage.

Without overmodulation, if the output voltage vector is synthesized by using the space vector modulation (SVM) or PWM with third-harmonic injection, the maximum magnitude of the phase voltage vector is given by

$$\begin{aligned} V_{s,max,1} &= \frac{1}{\sqrt{3}} v_{bt} \\ V_{s,max,2} &= \frac{1}{\sqrt{3}} v_{sc} \end{aligned} \quad (45)$$

The power density and energy capacities of the storage units have been selected in order to be compliant to the overall power of the IMD system, [4].

The current control loops bandwidth of the drives have been set to 420 Hz.

Fig. 10 displays the waveforms of electrical and mechanical quantities during an acceleration starting from the initial conditions reported in Fig. 11, where the status of the HESS and mechanical system are listed, as well as that of the boundary current limits and models parameters. For the sake of an easy exposition, we have assumed a transient at constant torque $T_{e,demand} = \text{const}$. The power delivered to the mechanical system has been split according to SOC and PC of both storages. This working condition is represented with a circular marker in the $i_{qs}-i_{ds}$ plane of Fig. 12, displaying the curve representing all the possible current sets (i_{qs}, i_{ds}) able to provide the same $T_{e,demand}$.

In order to verify whether the proposed method approaches the minimum losses conditions, the same IMD has been simulated considering an identical scenario but imposing different combinations of i_{qs1} , i_{qs2} , i_{ds1} , and i_{ds2} to the current control loops of the SMs, featuring the same $T_{e,demand}$. The results are shown in Fig. 13, grouped into three different total current sets (i_{qs}, i_{ds}) one of which is the MTPA condition given by (37) whose surface is labeled in Fig. 13 with a triangle; the surface labeled with a circle ($i_{qs} = 2.35$ A, $i_{ds} = 2.02$ A) is the one facing the minimum system losses. Although the losses have been displayed as a function of the qd axis currents associated to SM₁, they can be referred to the qd axis currents of SM₂ by considering the relationship (27).

The results clearly show that the proposed technique allows us to approach the minimum losses point, whose deviation has been experienced to be lower than 4% for the considered IMD. Moreover, under the MTPA condition, the current set i_{qs1}^* , i_{qs2}^* , i_{ds1}^* , and i_{ds2}^* computed by (37) provides the minimum losses, as displayed in Fig. 14.

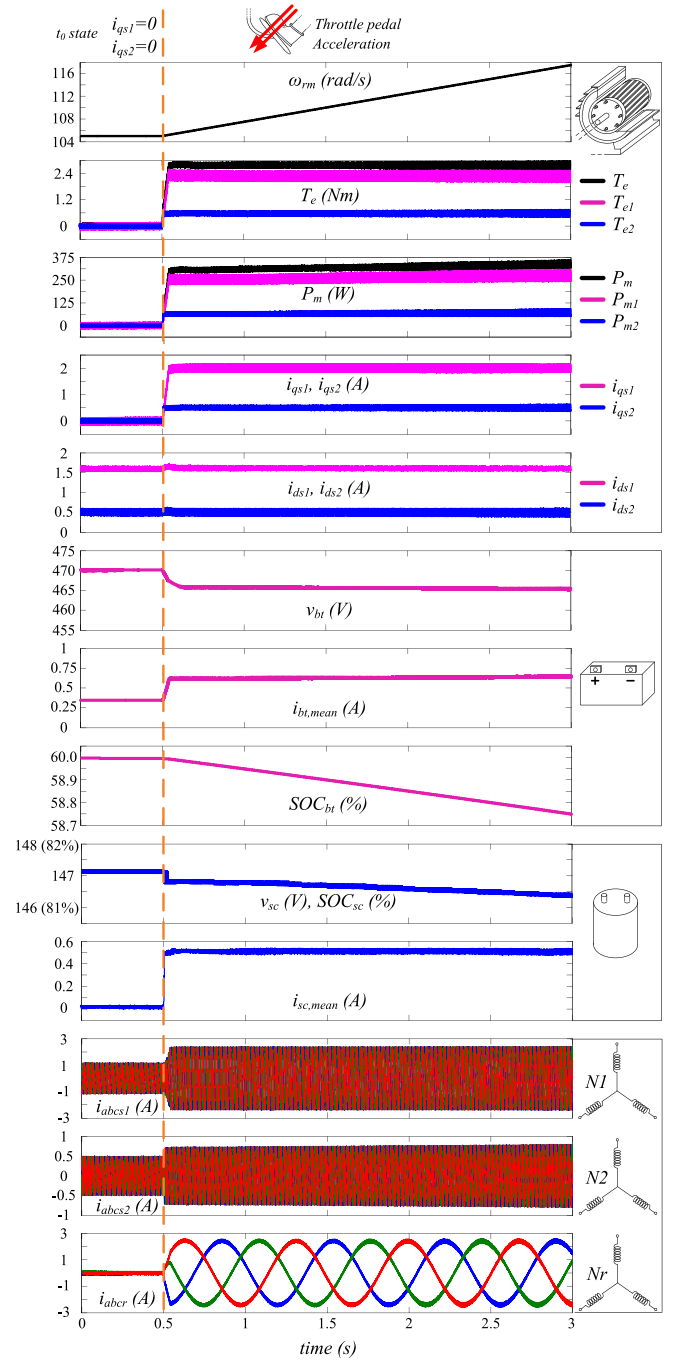


Fig. 10. Electrical and mechanical quantities during an acceleration scenario.



 Battery (bt)	$SOC_{bt}=60\%$ $SOC_{bt,min}=50\%$ $v_{bt,min}=400$ V	$i_{bt,ds,PC} \gg 10$ A $PC_{bt,ds} \gg 2$ kW $i_{qs1,limir} \gg 20$ A	Time horizon $\Delta t = 10$ s $\omega_{rm,\Delta t} = 105$ rad/s $R_{bt}(SOC=60\%) = 4.65$ Ω $K_{bt} = 0.25$ $K_{sc} = 0.86$ $K_I = 5.562$ $K_2 = 10.074$ $i_{ds,rate} = 2.34$ A
	 Supercap (sc)	$SOC_{sc}=82\%$ $SOC_{sc,min}=40\%$ $v_{sc,max}=160$ V	

Fig. 11. Status of the HESS and mechanical system, boundary current limits, and models parameters considered for the simulated acceleration scenario.

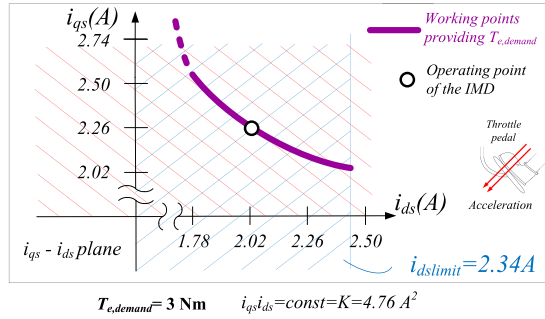


Fig. 12. Locus of currents set providing the demanded torque during the acceleration scenario.

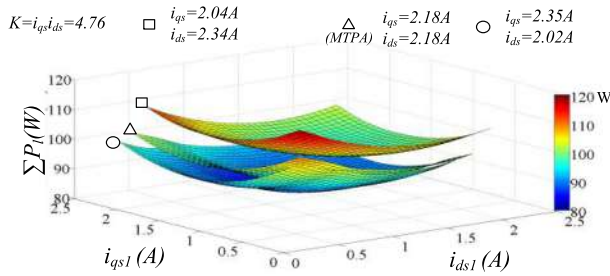


Fig. 13. Power losses computed by simulation executed at different combinations of i_{qs1} , i_{qs2} , i_{ds1} , and i_{ds2} .

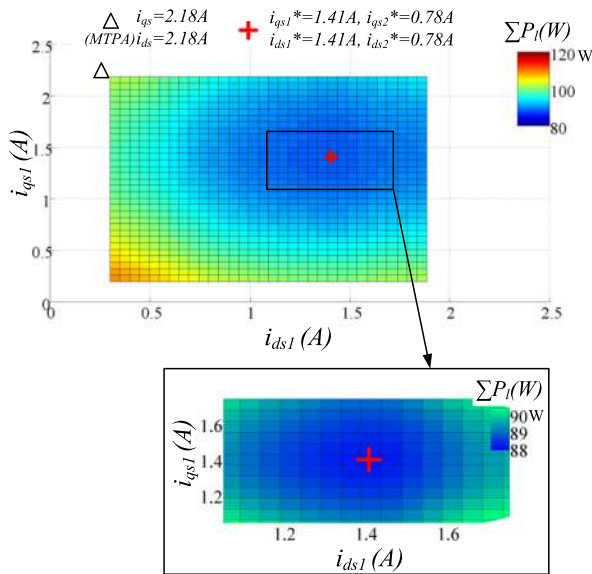


Fig. 14. Zoomed view of the power losses surface obtained in simulation under MTPA (Δ) condition.

Whenever the torque loads impose rated flux conditions, the relationship (38) must be used to carry out the optimal current set, in which i_{ds1} and i_{ds2} are equal to their respective rated values. Fig. 15 displays a different acceleration scenario, in which a much higher torque demand is required. It can be observed that even in these conditions the proposed method leads to the minimum of the IMD losses.

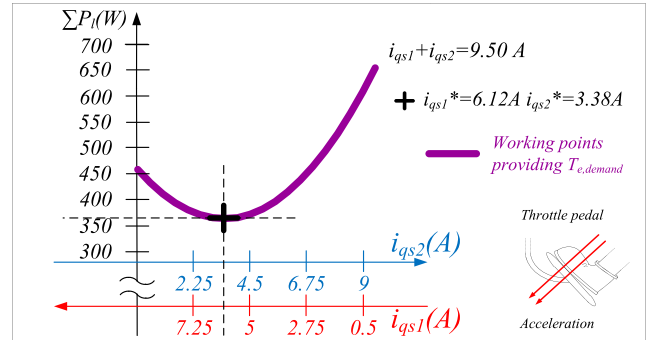


Fig. 15. Power losses versus torque current components providing the demanded torque and optimal operating point, determined according to (38).

Fig. 15. Power losses versus torque current components providing the demanded torque and optimal operating point, determined according to (38).

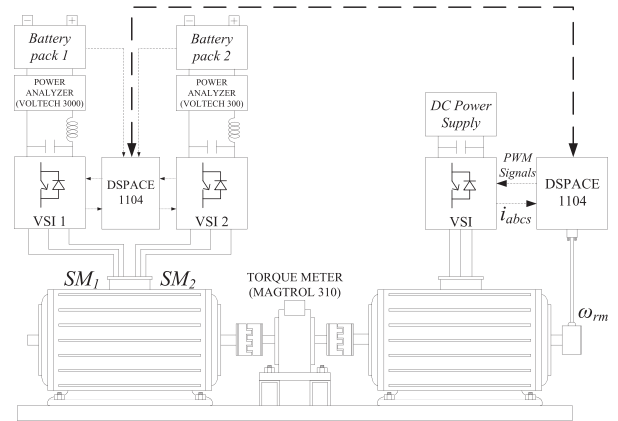


Fig. 16. Schematical representation of the test rig.

B. Experimental Results

In order to experimentally verify the effectiveness of the proposed losses minimization algorithm, some tests have been conducted on the test rig whose schematic diagram is displayed in Fig. 16 and image depicted in Fig. 17. The multiwinding electrical machine is the same of that considered in the simulations. The storage unit 1 is a 156-V 27-A·h VRLA battery pack, whereas the storage unit 2 consists of a 108-V 27-A·h VRLA battery pack. The drivetrain is mechanically coupled to a 3-kW induction motor drive in which an IFOC is implemented to impose the operating speed profile of the controlled IMD. The power losses at the terminals of the storage units have been measured by using a Voltech 300 and a Voltech 3000 digital power analyzers, whereas the measure of the motor phase voltages in both SMs is indirectly performed from the signals outgoing from the PI current controllers, suitably scaled according to the voltage measured at the terminals of the storage units and modulation strategy, SVM in this case [43].

The switching frequency of both inverters is 20 kHz, and a dead time equal to $1 \mu\text{s}$ has been included in the switching patterns of the modulators. Inverter nonlinearities have been compensated according to [44]–[48]. An electrolytic capacitor bank of $235 \mu\text{F}$ has been connected parallel at the dc terminals

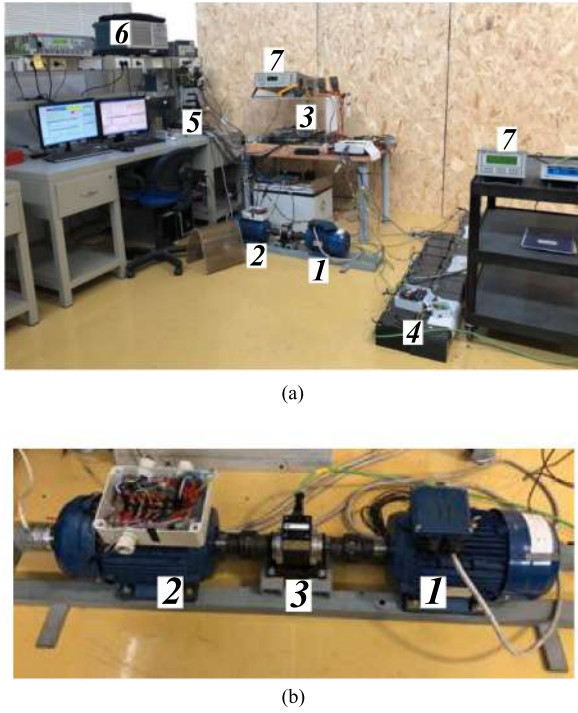


Fig. 17. (a) Test rig: (1) mechanical load—3-kW induction motor drive, (2) multiwinding induction machine, (3) voltage source inverters, (4) VRLA battery packs, (5) dSPACE control unit, (6) scope, and (7) power analyzers. (b) Drivetrain: (1) mechanical load—3-kW induction motor drive, (2) multiwinding induction machine, and (3) torque meter.

of each inverter. A torque meter Magtrol 310 has been used to measure the torque, whereas the rotor speed ω_{rm} is determined by applying a phase locked loop algorithm to the rotor position measured through a 5000 ppr incremental encoder.

The temperature of the winding and storage units has been monitored by using an infrared thermometer Fluke 561, which is used to measure the rise rating of the temperature above ambient of the motor case.

The resistive parameters values have been referred to the operating temperature. Both drives have been controlled by DSPACE 1104 development control boards, whose algorithms have been executed at $200 \mu\text{s}$. The current control loops bandwidth of the drives has been set to 420 Hz; the current control loops do not include feedforward decoupling terms.

Initially, some tests have been performed in order to verify the performances of the FOC strategy implemented in the drives composing the IMD.

The test displayed in Fig. 18 has been executed to evaluate the dynamic behavior of the decoupled torque and flux controls of the IFOCs implemented in the two SMs. In particular, the drives are torque controlled and square wave variations are imposed to the torque components $i_{qs1} = 1.8 \text{ A}$ and $i_{qs2} = 8 \text{ A}$, keeping constant the d -axis current components $i_{ds1} = 1.8 \text{ A}$ and $i_{ds2} = 0.5 \text{ A}$. It is worth noting that a satisfying transient behavior is achieved and field orientation is confirmed by the triangular waveform of the angular speed.

The experimental result of Fig. 19 has been acquired while operating both drives at steady state and rated conditions. The

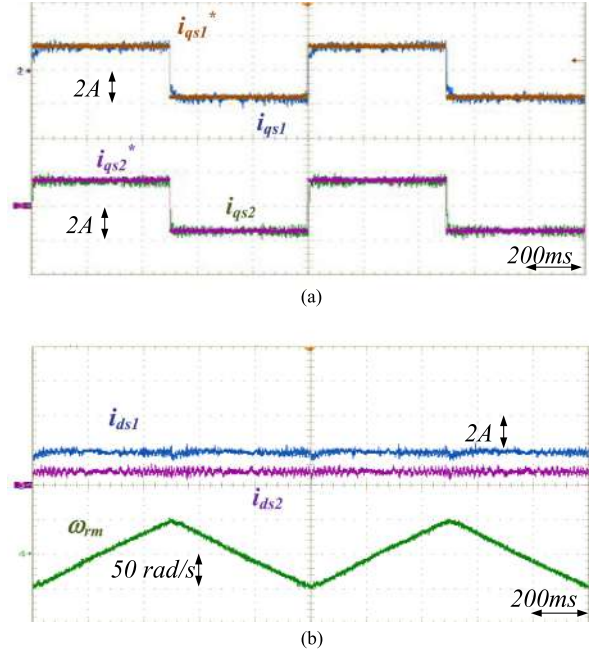


Fig. 18. Electrical and mechanical quantities of the IMD, measured during square wave torque variations.

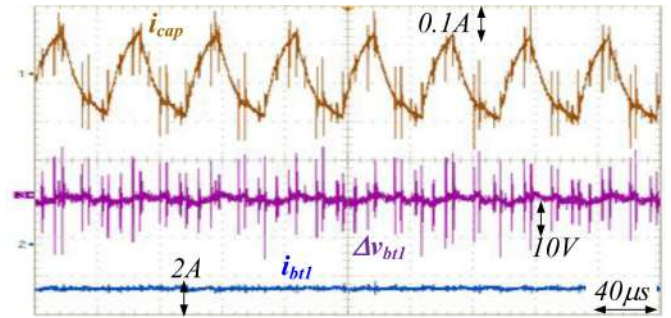


Fig. 19. Steady-state test: DC bus capacitors i_{cap} , the battery pack current i_{bt1} , and the ripple voltage measured at the terminals of the battery pack of the drive unit 1 Δv_{bt1} .

figure shows the currents flowing through the dc bus capacitors i_{cap} , the battery pack current i_{bt1} , and the ripple voltage measured at the terminals of the battery pack of the drive unit 1 Δv_{bt1} . This result is consistent with the hypothesis that limited losses can be associated to the dc bus capacitors as limited high frequency current ripple flows to such capacitors. High-frequency noise produced by the switching transitions of power devices is visible and superimposed to the traces.

The following experimental tests have been focused on a “Braking” scenario according to Fig. 6, in which the storage units are recharged through the regenerative power coming from the mechanical system. Fig. 20 summarizes the initial conditions of the HESS and mechanical system, the boundary current limits, and the models parameters.

The test bench has been operated imposing different combinations of i_{qs1} , i_{qs2} , i_{ds1} , and i_{ds2} to the current control loops of the SMs, featuring the same $T_{e,demand}$ in MTPA conditions $i_{qs} = 2.18 \text{ A}$ and $i_{ds} = 2.18 \text{ A}$ and same deceleration profile.

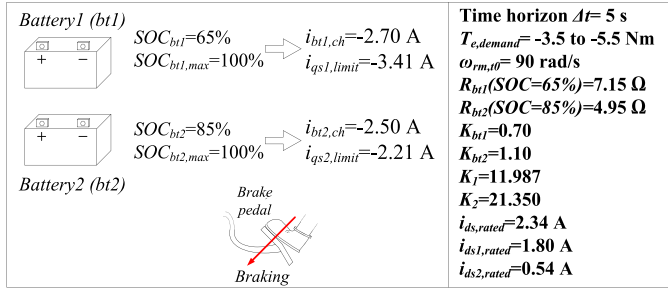


Fig. 20. Status of the HESS and mechanical system, boundary current limits, and model parameters for the considered experimental braking scenario.

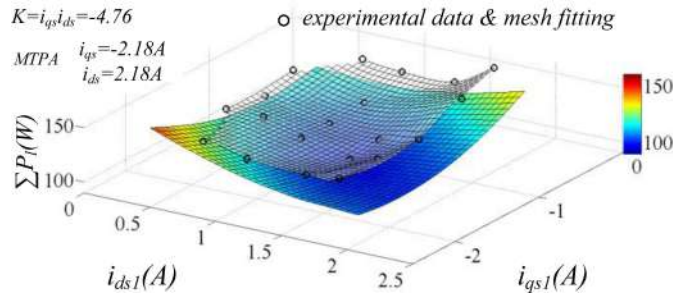


Fig. 21. Braking scenario: Power losses measured during experimental tests (gray mesh) and computed from simulation results (colored three-dimensional (3-D) plot), performed at different combinations of i_{qs1} , i_{qs2} , i_{ds1} , and i_{ds2} under MTPA conditions.

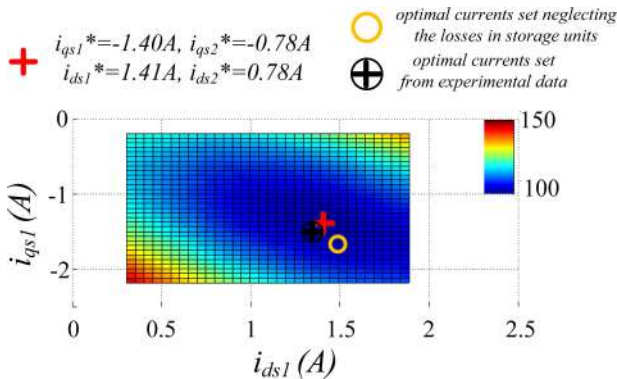


Fig. 22. Braking scenario: Zoomed view of the power losses surfaces obtained by simulations under MTPA condition with and without storage units. Optimal currents set from experiments is also indicated.

The experimental results of these tests are reported in Fig. 21 as a gray mesh interpolating the measured data. In the same figure, the colored three-dimensional (3-D) plot is obtained by simulating the IMD system. An offset between the two surfaces can be noted which would probably be caused by the mechanical and power converter losses that have been neglected in the theoretical analysis. Anyway, it is important to highlight that the optimal i_{qs1}^* , i_{qs2}^* , i_{ds1}^* , and i_{ds2}^* currents set, calculated by using the proposed method, is very close to the currents set corresponding to the minimum losses point identified by experimental data, as highlighted in Fig. 22.

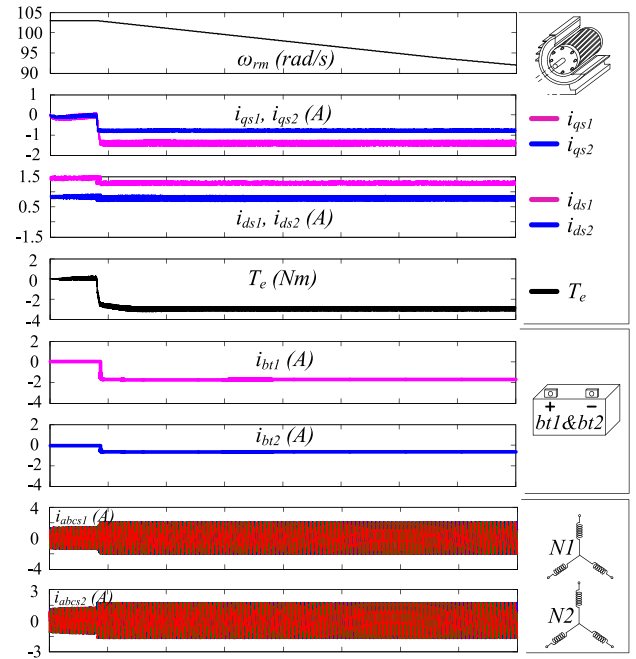


Fig. 23. Simulation results by considering the drive operated at the currents set i_{qs1}^* , i_{qs2}^* , i_{ds1}^* , and i_{ds2}^* indicated in Fig. 22.

The optimal currents set carried out by neglecting the losses associated to the storage units has been also calculated by the simulations and reported in the same figure. It can be noted that in the latter case, a more significant deviation can be observed in comparison to the experimental data. This will result in an increment of power losses equal to 22% compared to the experimental data when the losses of storage units are neglected. Conversely, the increment of power losses is limited to the 16% with respect to that provided by the experimental data when the losses of storage units are included. Such circumstance confirms the effectiveness of the proposed energy management strategy in which the losses in storage units are taken into account.

The tests reported in Figs. 23 and 24 compare the simulation and experimental results with the IMD operated at the i_{qs1}^* , i_{qs2}^* , i_{ds1}^* , and i_{ds2}^* currents set indicated in Fig. 22. It can be observed that a satisfactory matching between simulation and experimental results is obtained.

After having experimentally verified the proposed losses minimization strategy under the MTPA, the drive has been operated at rated flux value for four different values of the requested torques, at the same rotational speed $\omega_r = 90$ rad/s and same batteries SOC. The results are shown in Fig. 25. The system power losses have been measured for different combinations of i_{qs1} and i_{qs2} , and demanded torques as the difference between the mechanical power measured at the shaft of the electrical machine and the electrical power measured at batteries terminals. The efficiency η is evaluated referring to these power quantities. The same threshold values of Fig. 20 have been considered for the q -axis currents.

The minimum losses are reached for a couple of i_{qs1} and i_{qs2} , which is very close to that analytically provided by (38), i_{qs1}^* and i_{qs2}^* , confirming the validity of the proposed approach

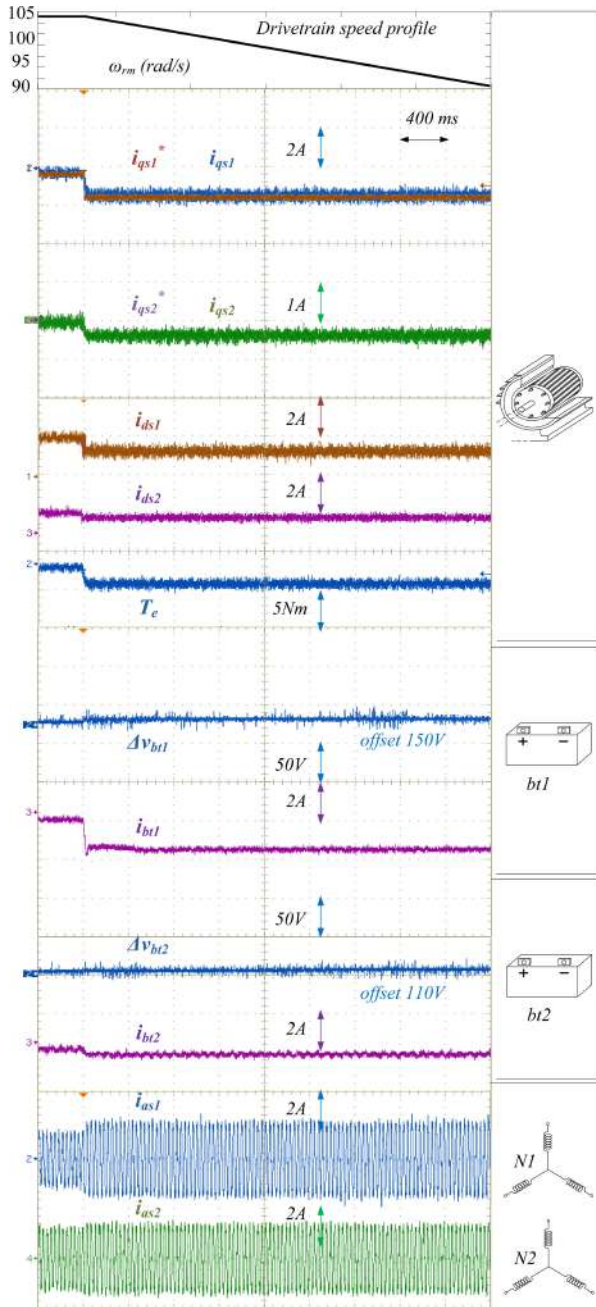


Fig. 24. Experimental test by considering the drive operated at the currents set i_{qs1}^* , i_{qs2}^* , i_{ds1}^* , and i_{ds2}^* indicated in Fig. 22.

to lead the IMD toward a very high efficiency operation for different operational scenario.

Looking at each figure, an offset between the two minimum losses points, experimental versus analytical calculation (38), can be noted.

This discrepancy would probably be caused by the mechanical and power converter losses that in the theoretical analysis have been neglected.

In Fig. 26, the overall power losses measured for each operating point of Fig. 25(d) have been split to evaluate each single losses contribution related to the electric machine and storage

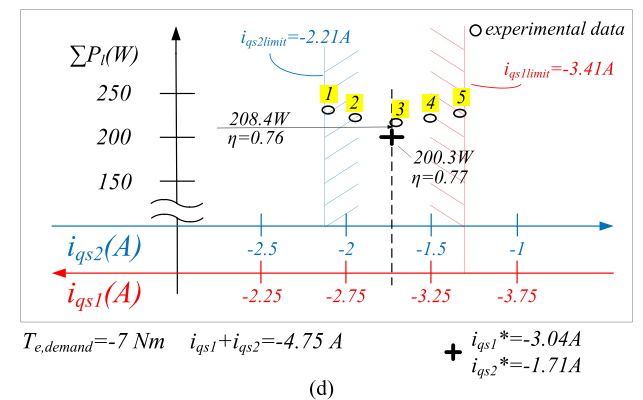
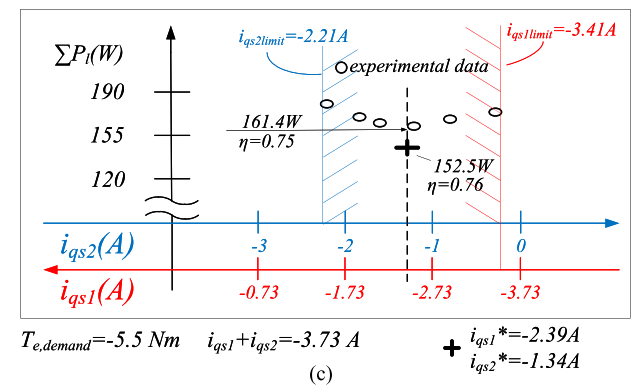
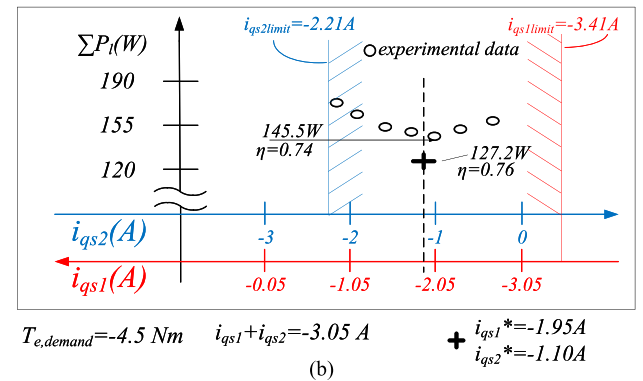
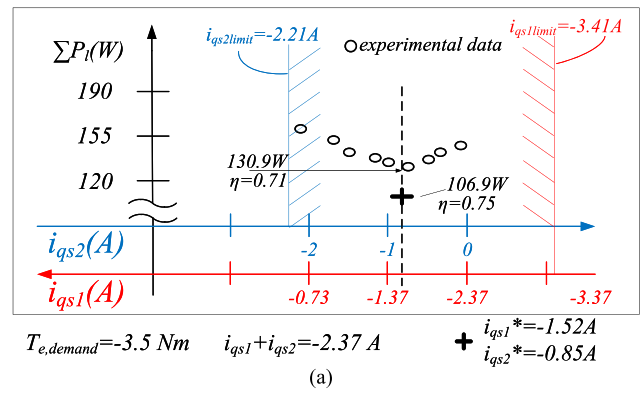


Fig. 25. Power losses versus torque current components providing the demanded braking torques and optimal operating points determined by (38).

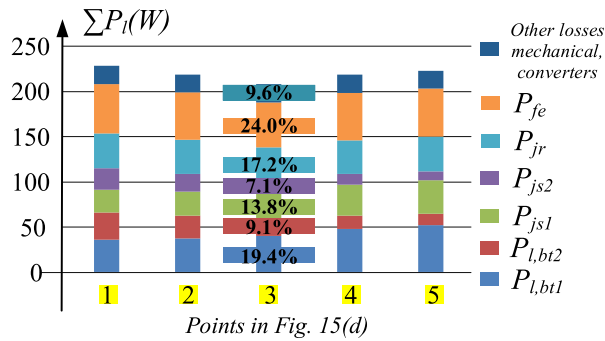


Fig. 26. Evaluation of each contribution to the overall power losses for each operating point in Fig. 25(d).

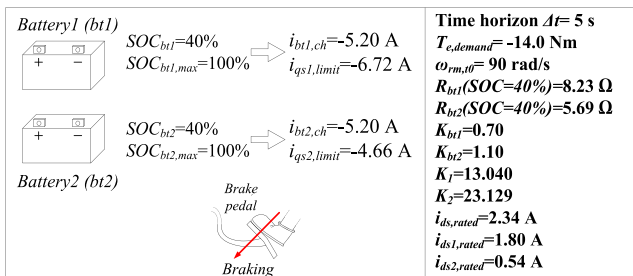


Fig. 27. Status of the HESS and mechanical system, boundary current limits, and model parameters of the tests for the experimental braking scenario of Fig. 28.

units. The system power losses have been measured as the difference between the mechanical power and the electrical power measured at batteries terminals. The losses in the stator windings have been evaluated by using the analytical expressions (17) and (18), whereas the joule losses in the rotor have been determined by using (19). Equation (28) has been exploited to calculate the iron losses. The losses associated with the batteries have been calculated according to (14).

Referring to the optimal operating point, it can be observed that the impact of joule losses of the induction machine is about 38%, whereas the percentage related to the iron losses is 24%.

Mechanical and converter losses have been extrapolated by the power balance in the system. The losses associated with the storage units are significant and equal to 28.5% of the total IMD losses. In other words, if the latter losses are neglected, the error in terms of power losses evaluation for the entire system is around 25%–30%.

Finally, the experimental test of Fig. 28 has been determined by setting the HESS status and IMD according to Fig. 27. Different than the previous tests, in such a case, the batteries SOC is very low, leading to a very large PC; therefore, the boundaries imposed for q -axis currents allow us to reach the rated torque. The optimal currents set determined by neglecting the losses associated with the storage units has also been shown in Fig. 28.

You can note a power losses deviation around 25% between the last operating point and the minimum losses point coming from experimental data.

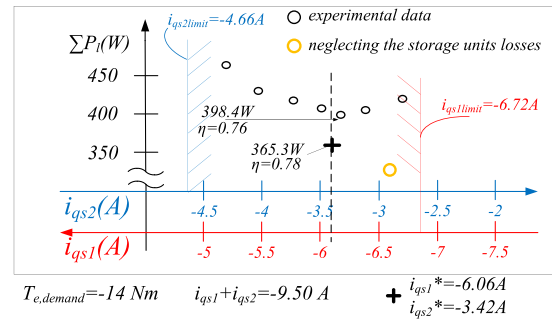


Fig. 28. Power losses versus torque current components providing the demanded braking torques, and optimal operating points determined according to (38).

VI. CONCLUSION

Addressing automotive applications, the potentiality of using IMD topologies and different energy storage units was highlighted in this paper. In particular, it demonstrated that the higher degrees of freedom of an IMD can effectively increase the flexibility and efficiency of the drive system. Although the study was focused on HEV parallel drivetrains, many other applications can be considered.

Experimental tests confirmed good agreement with the theoretical study, the last obtained by combining a very effective modeling of the induction machine and storage units, including technical constraints given by the PC and SOC. Although the optimal current profiles used in the current vector control loops of the IMD were obtained considering an MTPA curve for the global qd current quantities, nothing prevent the approach to be used considering different energy saving strategies.

REFERENCES

- [1] J. P. F. Trovao, V. D. N. Santos, C. H. Antunes, P. G. Pereirinha, and H. M. Jorge, "A real-time energy management architecture for multisource electric vehicles," *IEEE Trans. Ind. Electron.*, vol. 62, no. 5, pp. 3223–3233, May 2015.
- [2] A. Castaings, W. Lhomme, R. Trigui, and A. Bouscayrol, "Comparison of energy management strategies of a battery/supercapacitors system for electric vehicle under real-time constraints," *Appl. Energy*, vol. 163, pp. 190–200, Feb. 2016.
- [3] Z. Song, H. Hofmann, J. Li, J. Hou, X. Han, and M. Ouyang, "Energy management strategies comparison for electric vehicles with hybrid energy storage system," *Appl. Energy*, vol. 134, pp. 321–331, Dec. 2014.
- [4] X. Hu, J. Jiang, B. Egardt, and D. Cao, "Advanced power-source integration in hybrid electric vehicles: Multicriteria optimization approach," *IEEE Trans. Ind. Electron.*, vol. 62, no. 12, pp. 7847–7858, Dec. 2015.
- [5] J. O. Estima and A. J. M. Cardoso, "Efficiency analysis of drive train topologies applied to electric/hybrid vehicles," *IEEE Trans. Veh. Technol.*, vol. 61, no. 3, pp. 1021–1031, Mar. 2012.
- [6] W. Shabbir and S. A. Evangelou, "Real-time control strategy to maximize hybrid electric vehicle powertrain efficiency," *Appl. Energy*, vol. 135, pp. 512–522, Dec. 2014.
- [7] J. Kessels, M. Koot, P. van den Bosch, and D. Kok, "Online energy management for hybrid electric vehicles," *IEEE Trans. Veh. Technol.*, vol. 57, no. 6, pp. 3428–3440, Nov. 2008.
- [8] R. H. Nelson and P. C. Krause, "Induction machine analysis for arbitrary displacement between multiple winding sets," *IEEE Trans. Power Appl. Syst.*, vol. PAS-93, no. 3, pp. 841–848, May 1974.
- [9] H. Stemmler and R. Deplazes, "Multistar induction motors fed by voltage source inverters," in *Proc. Power Convers. Conf.*, 1997, vol. 1, pp. 119–126.

- [10] A. R. Munoz and T. A. Lipo, "Dual stator winding induction machine drive," *IEEE Trans. Ind. Appl.*, vol. 36, no. 5, pp. 1369–1379, Sep./Oct. 2000.
- [11] R. Bojoi, M. Lazzari, F. Profumo, and A. Tenconi, "Digital field-oriented control for dual three-phase induction motor drives," *IEEE Trans. Ind. Appl.*, vol. 39, no. 3, pp. 752–760, May/June 2003.
- [12] A. Tessarolo and C. Bassi, "Stator harmonic currents in VSI-fed synchronous motors with multiple three-phase armature windings," *IEEE Trans. Energy Convers.*, vol. 25, no. 4, pp. 974–982, Dec. 2010.
- [13] I. Zoric, M. Zabaleta, M. Jones, and E. Levi, "Techniques for power sharing between winding sets of multiple three-phase machines," in *Proc. IEEE Workshop Elect. Mach. Des., Control Diagnosis*, 2017, pp. 208–215.
- [14] W. Cai, "Comparison and review of electric machines for integrated starter alternator applications," in *Proc. Conf. Rec. Ind. Appl. Conf. 39th IAS Annu. Meeting*, Oct. 2004, vol. 1, pp. 386–393.
- [15] F. Leonardi and M. Degner, "Integrated starter-generator based HEVs: A comparison between low and high voltage systems," in *Proc. Rec. IEEE Int. Elect. Mach. Drives Conf.*, 2001, pp. 622–628.
- [16] M. Ehsani, G. Yimin, and J. M. Miller, "Hybrid electric vehicles: Architecture and motor drives," *Proc. IEEE*, vol. 95, no. 4, pp. 719–728, Apr. 2007.
- [17] H. Rehman, "An integrated starter-alternator and low-cost high-performance drive for vehicular applications," *IEEE Trans. Veh. Technol.*, vol. 57, no. 3, pp. 1454–1465, May 2008.
- [18] A. K. Jain, S. Mathapati, V. T. Ranganathan, and V. Narayanan, "Integrated starter generator for 42-V powertrain using induction machine and direct torque control technique," *IEEE Trans. Power Electron.*, vol. 21, no. 3, pp. 701–710, May 2006.
- [19] A. J. Zhang and M. F. Rahman, "A direct-flux-vector-controlled induction generator with space-vector modulation for integrated starter alternator," *IEEE Trans. Ind. Electron.*, vol. 54, no. 5, pp. 2512–2520, Oct. 2007.
- [20] S. Jurkovic, K. M. Rahman, J. C. Morgante, and P. J. Savagian, "Induction machine design and analysis for general motors e-assist electrification technology," *IEEE Trans. Ind. Appl.*, vol. 51, no. 1, pp. 631–639, Jan./Feb. 2015.
- [21] D. J. Perreault, K. K. Afridi, and I. A. Khan, "Automotive applications of power electronics," in *The Power Electronics Handbook*. M. H. Rashid, ed. New York, NY, USA: Academic, 2001, pp. 791–813.
- [22] F. Chai, S. Cui, and S. Cheng, "Performance analysis of double-stator starter generator for the hybrid electric vehicle," *IEEE Trans. Magn.*, vol. 41, no. 1, pp. 484–487, Jan. 2005.
- [23] G. Nobile, G. Scelba, M. Cacciato, and G. Scarcella, "Losses minimization control for an integrated multidrives topology devoted to hybrid electric vehicles," in *Proc. 43rd Annu. Conf. IEEE Ind. Electron. Soc.*, 2017, pp. 2059–2066.
- [24] G. Scarcella, G. Scelba, M. Cacciato, A. Spampinato, and M. M. Harbaugh, "Vector control strategy for multidirectional power flow in integrated multidrives starter-alternator applications," *IEEE Trans. Ind. Appl.*, vol. 52, no. 6, pp. 4816–4826, Dec. 2016.
- [25] E. Levi, "Multiphase electric machines for variable-speed applications," *IEEE Trans. Ind. Electron.*, vol. 55, no. 5, pp. 1893–1909, May 2008.
- [26] D. Rotenberg, A. Vahidi, and I. Kolmanovskiy, "Ultracapacitor assisted powertrains: modeling, control, sizing, and the impact on fuel economy," *IEEE Trans. Control Syst. Technol.*, vol. 19, no. 3, pp. 576–589, May 2011.
- [27] S. M. Mousavi and M. Nikdel, "Various battery models for various simulation studies and applications," *Renewable Sustain. Energy Rev.*, vol. 32, pp. 477–485, Apr. 2014.
- [28] M. Cacciato, G. Nobile, G. Scarcella, G. Scelba, and A. G. Sciaccia, "Energy management optimization in stand-alone power supplies using online estimation of battery SOC," in *Proc. 18th Eur. Conf. Power Electron. Appl.*, 2016, pp. 1–10.
- [29] G. L. Plett, "High-performance battery-pack power estimation using a dynamic cell model," *IEEE Trans. Veh. Technol.*, vol. 53, no. 5, pp. 1586–1593, Sep. 2004.
- [30] N. Achaibou, M. Haddadi, and A. Malek, "Lead acid batteries simulation including experimental validation," *J. Power Sources*, vol. 185, pp. 1484–1491, Dec. 2008.
- [31] S. Lim and K. Nam, "Loss-minimizing control scheme for induction motors," *IEEE Trans. Elect. Power Appl.*, vol. 151, no. 4, pp. 385–397, Jul. 2004.
- [32] Z. Qu, M. Ranta, M. Hinkkanen, and J. Luomi, "Loss-minimizing flux level control of induction motor drives," *IEEE Trans. Ind. Appl.*, vol. 48, no. 3, pp. 952–961, May/June 2012.
- [33] J. Stumper, A. Dötlinger, and R. Kennel, "Loss minimization of induction machines in dynamic operation," *IEEE Trans. Energy Convers.*, vol. 28, no. 3, pp. 726–735, Sep. 2013.
- [34] K. Marouani, M. Nesri, and K. Nounou, "Rotor flux control with copper losses reduction in a high power drive system," in *Proc. IEEE Int. Power Electron. Motion Control Conf.*, 2016, pp. 700–705.
- [35] A. Wang and Z. Ling, "Realization of vector control for induction motor considering iron loss," in *Proc. IEEE Int. Symp. Intell. Inf. Technol. Appl.*, 2008, pp. 761–765.
- [36] L. Rambaldi, E. Bocci, and F. Orecchini, "Preliminary experimental evaluation of a four wheel motors, batteries plus ultracapacitors and series hybrid powertrain," *Appl. Energy*, vol. 88, pp. 442–448, Feb. 2011.
- [37] Y. Jeong, S. Sul, S. Hiti, and K. M. Rahman, "Online minimum-copper-loss control of an interior permanent-magnet synchronous machine for automotive applications," *IEEE Trans. Ind. Appl.*, vol. 42, no. 5, pp. 1222–1229, Sep./Oct. 2006.
- [38] D. Casadei, M. Mengoni, G. Serra, A. Tani, and L. Zarri, "A control scheme with energy saving and DC-Link overvoltage rejection for induction motor drives of electric vehicles," *IEEE Trans. Ind. Appl.*, vol. 46, no. 4, pp. 1436–1446, Jul./Aug. 2010.
- [39] S. Bozhko, S. Dymko, S. Kovbasa, and S. M. Paresada, "Maximum torque-per-amp control for traction im drives: theory and experimental results," *IEEE Trans. Ind. Appl.*, vol. 53, no. 1, pp. 181–193, Feb. 2017.
- [40] W. Sung, J. Shin, and Y. Jeong, "Energy-efficient and robust control for high-performance induction motor drive with an application in electric vehicles," *IEEE Trans. Veh. Technol.*, vol. 61, no. 8, pp. 3394–3405, Oct. 2012.
- [41] G. O. Garcia, J. C. M. Luis, R. M. Stephan, and E. H. Watanabe, "An efficient controller for an adjustable speed induction motor drive," *IEEE Trans. Ind. Electron.*, vol. 41, no. 5, pp. 533–539, Oct. 1994.
- [42] D. Feroldi and M. Carignano, "Sizing for fuel cell/supercapacitor hybrid vehicles based on stochastic driving cycles," *Appl. Energy*, vol. 183, pp. 645–658, Dec. 2016.
- [43] J. Holtz, "Pulsewidth modulation—A survey," *IEEE Trans. Ind. Electron.*, vol. 39, no. 5, pp. 410–420, Oct. 1992.
- [44] H. Sedki and S. Djennoune, "Compensation method eliminating voltage distortions in PWM inverter," *Int. J. Elect., Comput., Electron. Commun. Eng.*, vol. 3, no. 6, pp. 1402–1409, 2009.
- [45] D.-M. Park and K.-H. Kim, "Parameter-independent online compensation scheme for dead time and inverter nonlinearity in IPMSM drive through waveform analysis," *IEEE Trans. Ind. Electron.*, vol. 61, no. 2, pp. 701–707, Feb. 2014.
- [46] A. Gaeta, P. Zanchetta, F. Tinazzi, and M. Zigliotto, "Advanced self-commissioning and feed-forward compensation of inverter nonlinearities," in *Proc. IEEE Int. Conf. Ind. Technol.*, 2015, pp. 610–616.
- [47] N. Bedetti, S. Calligaro, and R. Petrella, "Accurate modeling, compensation and self-commissioning of inverter voltage distortion for high-performance motor drives," in *Proc. IEEE Appl. Power Electron. Conf. Expo.*, 2014, pp. 1550–1557.
- [48] M. Schubert and R. W. De Doncker, "Instantaneous phase voltage sensing in PWM voltage-source inverters," *IEEE Trans. Power Electron.*, vol. 33, no. 8, pp. 6926–6935, Aug. 2018.



Giovanni Nobile (S'18) was born in Ragusa, Italy, in 1983. He received the B.S. and M.S. degrees in electrical engineering from the University of Catania, Catania, Italy, in 2005 and 2007, respectively. He is currently working toward the Ph.D. degree in performance analysis of distributed power converters in automotive and renewable energies with the Department of Electric, Electronic and Computer Science, University of Catania.

In 2007, he joined some international companies where he was involved in the field of power generation from renewables working on plant design, high-voltage equipment, grid connection infrastructures, monitoring systems, operation, and maintenance. His research interests include energy storage systems, renewable energy power plants, power electronics, and electric drives.

Mr. Nobile is a member of the Italian Association of Electrical and Electronics Engineers (AEIT).



Giacomo Scelba (S'04–M'07–SM'17) was born in Caltagirone, Italy, in 1976. He received the M.S. and Ph.D. degrees in electrical engineering from the University of Catania, Catania, Italy, in 2002 and 2006, respectively.

He is currently an Assistant Professor with the Department of Electrical, Electronic Engineering and Computer Science (DIEEI), University of Catania. He is also the co-PI of a collaborative research agreement between the DIEEI and the Department of Astronautical, Electrical and

Energy Engineering, University of Rome "La Sapienza," for research in the field of wide-bandgap-semiconductor-based drives. His research activity was initially focused on sensorless control, digital signal processing, and ac drive control technologies, whereas his current research interests are toward fault-tolerant ac drive systems, control techniques for renewable energy systems, and advanced technologies for power electronics applications.

Prof. Scelba is a member of the IEEE INDUSTRY APPLICATIONS, the IEEE INDUSTRIAL ELECTRONICS, and the IEEE Power Electronics Societies. He is also a member of the IEEE IAS Industrial Drives Committee. He is currently an Associate Editor for the IEEE TRANSACTIONS ON INDUSTRY APPLICATIONS. He was the recipient of the 2014 First Prize Paper Award and the 2016 Third Prize Paper Award, both from the IAS Industrial Drives Committee.



Mario Cacciato (S'99–M'00) received the M.S. (*cum laude*) degree in electrical engineering from the University of Catania, Catania, Italy, in 1996, and the Ph.D. degree in electronic engineering from the University of Reggio Calabria, Reggio Calabria, Italy, in 2000.

In 2000, he became an Assistant Professor with the Department of Electrical Engineering, University of Rome "La Sapienza," Rome, Italy. In 2004, he was with the Department of Electrical, Electronics and Computer Engineering, Uni-

versity of Catania. Since 2011, he has been an Associate Professor with the Department of Electrical and Electronic Engineering and Informatics, University of Catania, where is currently teaching electrical machines. He is the author of more than 130 technical papers, published on journals and proceedings of international conferences. From 2016, he has been the coordinator of the master degree in electrical engineering of the University of Catania. His main scientific interests include topologies and control of power electronics and electric drives for automotive, storage, and renewable energies.

Prof. Cacciato is a Member of the IEEE INDUSTRIAL ELECTRONICS and the IEEE Power Electronics Societies. He is also a Member of the European Power Electronics Association (EPE) where he is currently a Member of the EPE Executive Council. He is currently an Associate Editor for the *EPE Journal—European Power Electronics and Drives* published by Taylor & Francis.



Giuseppe Scarcella (S'98–M'99–SM'17) received the M.S. and Ph.D. degrees in electrical engineering from the University of Catania, Catania, Italy, in 1995 and 1999, respectively.

In 1998, he was with the University of Wisconsin-Madison, Madison, WI, USA, working on sensorless control of electrical drives. In 1999, he joined the Department of Electrical, Electronic, and Systems Engineering, University of Catania, as a Temporary Researcher. In 2001 and 2005, he obtained permanent position as

an Assistant and Associate Professor, in the same department, where, since 2018, he has been a Full Professor in the areas of power electronics and electrical machines and drives. He is the author or coauthor of more than 190 technical papers published in journals and proceedings of national and international conferences and is a holder of several international patents. His current research interests include sensorless control of electrical machines, fault-tolerant control, digital modulation techniques, efficiency optimization techniques, and renewable energy.

Prof. Scarcella is a member of the Italian Electric Association (AEIT) and the Industrial Drives and Electrical Machines Committees. He is a member of Motor Drives and Actuators Committee of power electronics society (PELS) where, from 2011 to 2013, he was the Chairman of the sensorless control topic. From 2012 to 2015, he was an Associate Editor for the IEEE TRANSACTIONS ON INDUSTRY APPLICATIONS. He was the recipient of an award for the best paper published in the IEEE TRANSACTIONS ON POWER ELECTRONICS in 2000 and several Third Prize and Best Paper awards for papers presented at the IEEE Industry Applications Society and IEEE ENERGY CONVERSION CONGRESS AND EXPOSITION.